Spin-glass state in nanoparticulate $(La_{0.7}Sr_{0.3}MnO_3)_{1-x}$ $(BaTiO_3)_x$ solid solutions: Experimental and density-functional studies

Chiranjib Nayek,[1] S. Samanta,[1] Kaustuv Manna,[2] A. Pokle,[3] B. R. K. Nanda,[1] P. S. Anil kumar,[2] and P. Murugavel[1,*]

[1]*Department of Physics, Indian Institute of Technology Madras, Chennai-600036, India*

[2]*Department of Physics, Indian Institute of Science, Bangalore-560012, India*

[3]*Icon Analytical Equipment Pvt. Ltd., Worli, Mumbai-400042, India*

(Received 9 July 2015; revised manuscript received 18 January 2016; published 1 March 2016)

We report the transition from robust ferromagnetism to a spin-glass state in nanoparticulate $La_{0.7}Sr_{0.3}MnO_3$ through solid solution with $BaTiO_3$. The field- and temperature-dependent magnetization and the frequency-dependent ac magnetic susceptibility measurements strongly indicate the existence of a spin-glass state in the system, which is further confirmed from memory effect measurements. The breaking of long-range ordering into short-range magnetic domains is further investigated using density-functional calculations. We show that Ti ions remain magnetically inactive due to insufficient electron leakage from $La_{0.7}Sr_{0.3}MnO_3$ to the otherwise unoccupied Ti-*d* states. This results in the absence of a Mn-Ti-Mn spin exchange interaction and hence the breaking of the long-range ordering. Total-energy calculations suggest that the segregation of nonmagnetic Ti ions leads to the formation of short-range ferromagnetic Mn domains.

DOI: 10.1103/PhysRevB.93.094401

I. INTRODUCTION

$La_{1-x}Sr_xMnO_3$ is one of the most widely studied colossal magnetoresistance materials in the lanthanum manganite family [1,2]. The large Curie temperature [3] T_C (∼370 K) and strong spin-lattice-charge coupling [4] in this material pave ways for practical applications [2]. Recently, exotic magnetic phenomena have been explored in $La_{1-x}Sr_xMnO_3$-based compounds in the form of heterostructures, solid solutions, and nanocomposites [5–7]. Magnetoelectric coupling is envisaged in $La_{0.67}Sr_{0.33}MnO_3$-$BaTiO_3$ heterostructures [8] and $La_{0.8}Sr_{0.2}MnO_3$-$Pb(Zr_{0.2}Ti_{0.8})O_3$ nanocomposites [9]. Large low-field magnetoresistance is achieved in $La_{0.7}Sr_{0.3}MnO_3$-NiO composites [10]. Even a spin-glass- (SG-) like state is reported in $La_{0.7}Sr_{0.3}MnO_3$-$SrMnO_3$ heterostructures due to competing magnetic orders and spin frustration at the interface [11].

The SG phase is basically a random yet cooperative frozen spin state without any long-range ordering. The SG states reported in the majority of the systems exhibit low freezing temperatures, which hinders their application potential. In this context, the reports on SG-like behavior in manganites [12–16] and cobaltites [17,18] have drawn major attention. Interestingly, a reentrant SG state in a Ti-substituted manganite system is assigned to the increase of disorder in the system [15]. However, the ambiguity between the prevailing superparamagnetic, interparticle dipolar interaction and the spin-glass state in some of these systems still remains to be resolved. To get further insight into the SG state, we have chosen a $(La_{0.7}Sr_{0.3}MnO_3)_{1-x}$ $(BaTiO_3)_x$ solid solution with $x = 0.05, 0.08, 0.12$, and 0.25. The magnetic measurements reported in this paper confirm the SG states of the sol-gel-synthesized nanoparticulate single-phase $(La_{0.7}Sr_{0.3}MnO_3)_{1-x}$ $(BaTiO_3)_x$ solid solutions.

The origin of the SG state may be from the interaction between the uncompensated spins of neighboring nanoparticles arising from the finite-size effects where the magnetocrystalline anisotropy dominates [19]. The glassiness may also appear in dense particle systems due to the dipole-driven ferro- and ferrimagnetic ordering [20]. While the former requires a large value of the anisotropy energy [19] (effective uniaxial anisotropy constant K of the order of $\sim 10^4$ J m^{-3}), where in the $(La_{0.7}Sr_{0.3}MnO_3)_{1-x}$ $(BaTiO_3)_x$ system the value can be ignored (K ∼ 0.86–1.6 J m^{-3}), the latter additionally demands the particle size to be very small (<10 nm) [20]. However, the nanoparticles we present here are polycrystalline and of the size range 35–45 nm.

As conventional causes fail to explain the SG behavior in $(La_{0.7}Sr_{0.3}MnO_3)_{1-x}$ $(BaTiO_3)_x$, the process of magnetization in this system needs to be examined. It is well known that $La_{0.7}Sr_{0.3}MnO_3$ (LSMO) is a robust ferromagnet, where the partially occupied itinerant e_g states mediate the ferromagnetism [21] via a double-exchange mechanism [22]. Therefore, it is imperative to study the role of $BaTiO_3$ (BTO), particularly that of Ti, in breaking the long-range magnetic order. In this context we have carried out calculations based on density-functional theory (DFT) using the full-potential linearized augmented plane wave (FP-LAPW) method [23]. We found insufficient electron leakage from LSMO to the otherwise unoccupied Ti-*d* states to spin-polarize the latter. This leads to the absence of a Mn-Ti-Mn spin exchange interaction. The DFT study also suggests the effect of BTO in producing small LSMO domains as schematically shown in Fig. 1. While the domains are ferromagnetic, the spin orientation of each of them can be random and thus induce the SG behavior. Detailed experimental and DFT studies carried out on nanoparticulate single-phase $(LSMO)_{1-x}(BTO)_x$ solid solutions are discussed in this paper.

II. EXPERIMENTAL PROCEDURE

A series of $(LSMO)_{1-x}(BTO)_x$ ($x = 0$, 0.05, 0.08, 0.12, and 0.25) solid solutions are prepared by the sol-gel route. For the synthesis of LSMO nanoparticles, the gel is prepared

*muruga@iitm.ac.in

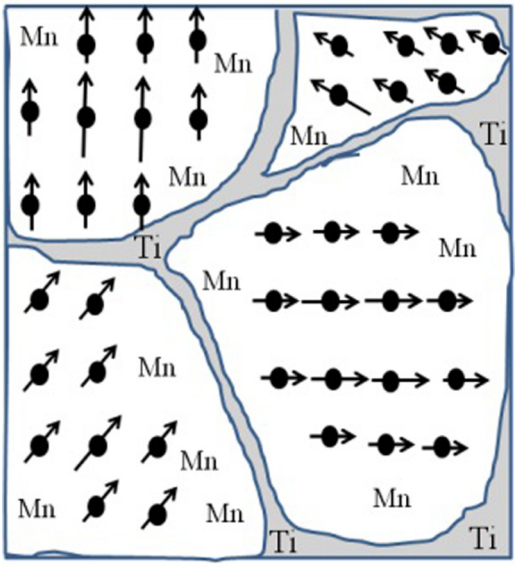

FIG. 1. Schematic illustration of spin-glass state in nanoparticulate $(LSMO)_{1-x}(BTO)_x$ solid solutions as predicted from the DFT calculations. Nonmagnetic Ti breaks the long-range spin ordering. Ti segregates to form short-range ferromagnetic Mn domains.

from the stoichiometric amounts of 0.05*M* lanthanum nitrate, manganese nitrate, and strontium nitrate by the citric acid route. The dried gel is preannealed at 450 °C for 2 h and finally annealed at 700 °C for 6 h to get the LSMO nanoparticles. To get the $(LSMO)_{1-x}(BTO)_x$ compound, appropriate amounts of 0.005*M* aqueous barium carbonate solution and titanium tetraisopropoxide in ethanol are added to 0.015*M* and 0.15*M* citric acid, respectively. These two solutions are mixed and maintained at room temperature by constantly stirring for 30 min to get the gel. Later, an appropriate amount of LSMO powder is added to the gel, sonicated for 1 h, and dried at 60 °C in a magnetic stirrer. The dried powders are then annealed at 780 °C for 5 h to form the $(LSMO)_{1-x}(BTO)_x$ nanoparticles. The powders are characterized using a PANanalytical X'Pert Pro x-ray diffractometer, a JEOL-made high-resolution transmission electron microscope (HRTEM), and a Lakeshore vibrating sample magnetometer (VSM) for their phase formation, morphologies, and magnetic properties, respectively. The ac susceptibility (χ_{ac}) measurements are performed using a commercial CryoBIND system down to 77 K with frequency in the range of 9 Hz to 1 kHz. The Rietveld refinements of the x-ray diffraction (XRD) data are done by the general structure analysis system (GSAS) code.

III. EXPERIMENTAL RESULTS

A. Structural and morphological analysis

The XRD patterns of $(LSMO)_{1-x}(BTO)_x$ for $x = 0, 0.05, 0.08, 0.12$, and 0.25 along with their Rietveld refinement data are shown in Fig. 2. The patterns confirm that the samples are in single phase without the trace of any secondary phases. The Rietveld refinement reveals that the samples undergo structural changes as we increase the concentration x. Initially, the parent LSMO is crystallized in

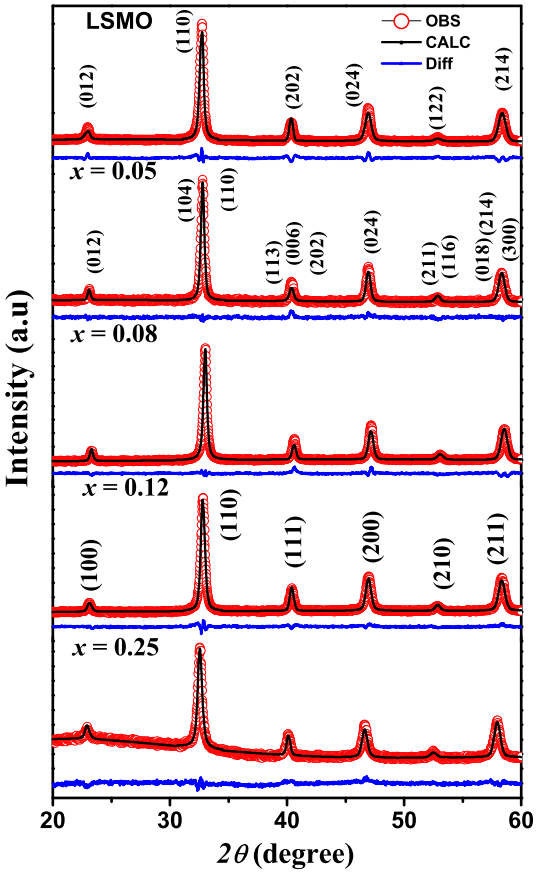

FIG. 2. XRD patterns and the refined plots for $(LSMO)_{1-x}(BTO)_x$ ($x = 0$, 0.05, 0.08, 0.12, and 0.25) samples.

the orthorhombic phase with *Pbnm* space group ($a = 3.864$ Å, $b = 3.852$ Å, and $c = 3.871$ Å); whereas upon doping, for $x = 0.05$ and 0.08, the compound crystallized in the rhombohedral phase ($a = 5.494$ Å, $c = 13.484$ Å, and $a = 5.502$ Å, $c = 13.458$ Å, respectively) with $R\bar{3}c$ space group. Finally, for $x = 0.12$ and above, the compound stabilized in the cubic phase with $Pm\bar{3}m$ space group.

The morphological studies of all the samples are done by HRTEM and, as a representative example, the microscopic image of the $x = 0.08$ sample is shown in Fig. 3(a). As seen from the figure, the particles are arbitrary in shape. The histogram shown in Fig. 3(b) reveals the particle size distribution with the maximum distribution between 35 and 45 nm. The selected area diffraction (SAED) done on a single particle and the corresponding HRTEM image are shown in Figs. 3(c) and 3(d), respectively. The ring pattern in the SAED data confirms the polycrystalline nature of the particles. The lattice spacing (d) estimated from the SAED pattern and the HRTEM image matches well with the XRD data.

B. Magnetic properties

To study the magnetic properties, the magnetization (M) is measured as a function of temperature (T) from 20 to 400 K under zero-field-cooled (ZFC) and field-cooled (FC) conditions in the field of 200 Oe for all samples and the results

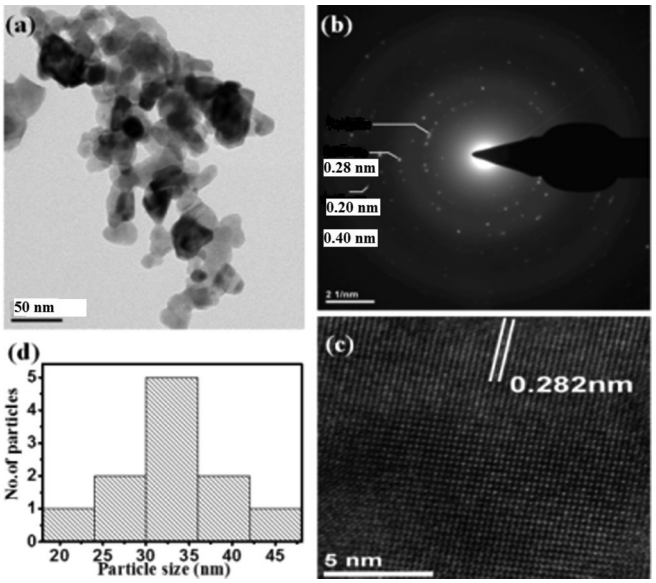

FIG. 3. (a) The microscopic image, (b) the SAED pattern, (c) the HRTEM image, and (d) the histogram of the $x = 0.08$ sample.

are shown in Fig. 4. The FC curves exhibit ferromagnetic like character where the compounds $x = 0, 0.05, 0.08, 0.12$, and 0.25 show T_C at 360, 310, 294, 285, and 259 K, respectively. The T_C is decreased with increase in Ti^{4+} content in the sample. The decrease in T_C may originate from the effect of dilution of the exchange interaction between Mn^{3+} and Mn^{4+} ions via oxygen, disorder induced by the doping at A- and B-site sublattices, and the change in the Mn^{3+}-O-Mn^{4+} bond angle in the system. The ZFC curve exhibits a cusp

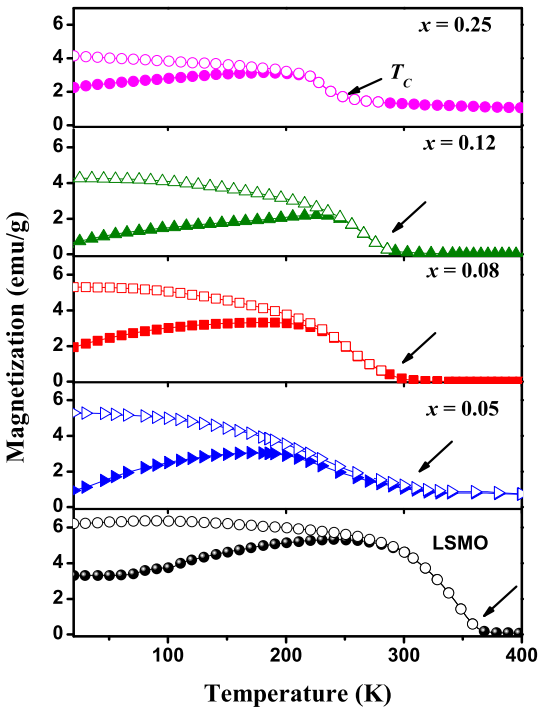

FIG. 4. M versus T measured at 200 Oe field for $x = 0.0, 0.05, 0.08, 0.12$, and 0.25 samples.

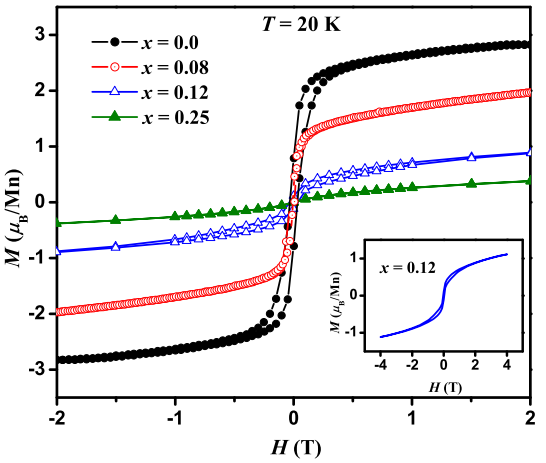

FIG. 5. M versus H curve plotted at 20 K for $x = 0, 0.08, 0.12$, and 0.25 up to 2 T.Inset shows the M-H curve for $x = 0.12$ sample up to 4 T.

below T_C and starts deviating from the FC plot down to low temperature.

M is measured as a function of magnetic field (H) at 20 K for all samples and the results are shown in Fig. 5 up to 2 T field. The magnetization values for $x = 0, 0.08, 0.12$, and 0.25 are 2.87, 2.00, 0.83, and 0.39 μ_B/Mn at 2 T, respectively. These values are lower as compared to the expected values of 3.67, 3.4, 3.25, and 2.78 μ_B/Mn for the corresponding samples. The observed low value of M for LSMO could be due to the particle size effect reported in the literature [24]. In addition, M shows a decreasing trend with x and an unsaturated moment even at 2 T. The decrease in magnetic moment could be the dilution effect of Mn atoms in the sublattice by nonmagnetic Ti^{4+} ions as suggested by the DFT results which will be discussed later. In comparison with the parent LSMO compound, the solid solution samples exhibit an unsaturated magnetic moment even at 4 T (see the inset of Fig. 5). The features observed in the M-T and M-H plots hint at the existence of possible glassiness in these systems.

C. ac magnetic susceptibility

To investigate the SG behavior further, the T-dependent ac susceptibility $\chi(T)$ is measured at different frequencies (f) ranging from 9 Hz to 1 kHz in a probing ac field (H_{ac}) of 0.17 Oe. The normalized $\chi'(T)$ (in-phase) components plotted from 77 to 300 K for $x = 0.05, 0.08, 0.12$, and 0.25 at different f (for clarity the plots are shown for three different frequencies) are presented in Figs. 6(a)–6(d), respectively. The samples show a broad peak (T_P) at 251, 266, 241 and 119 K for $x = 0.05, 0.08, 0.12$, and 0.25, respectively. The $\chi'(T)$ exhibit a f-dependent behavior around T_P. The T_P shifts to a lower value with the increase in f as highlighted in the inset of Fig. 6. This is a typical signature of a glassy magnetic interaction in the samples. However, unlike the usual canonical SG system, the samples show a reverse trend in T_P shift [25]. This may be due to the presence of both fast and slow spin relaxations in the freezing process associated with the short-range and long-range magnetic ordering, respectively. The decrease in

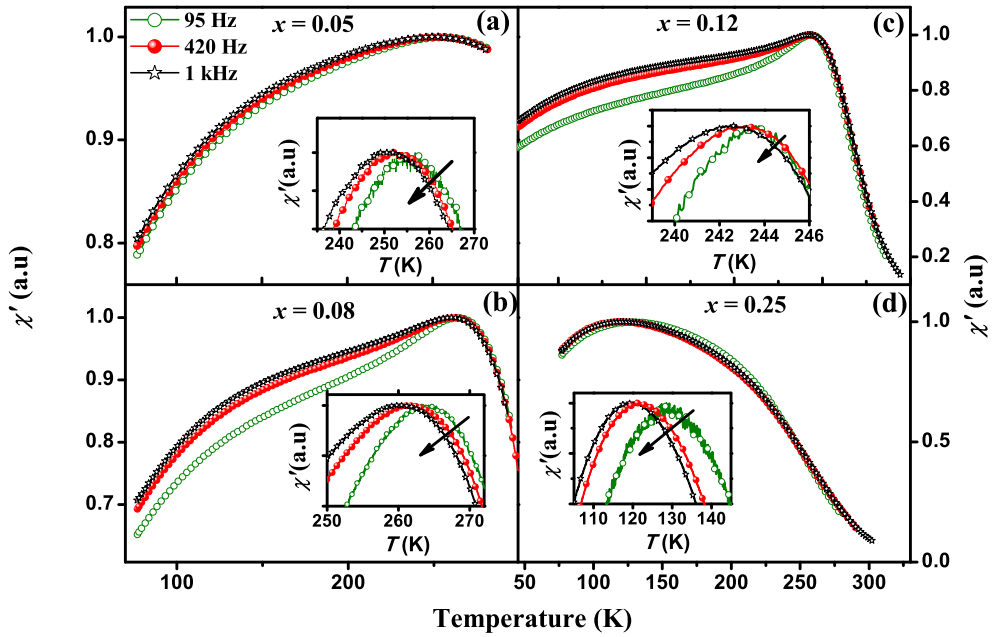

FIG. 6. Temperature-dependent ac susceptibility for x = (a) 0.05, (b) 0.08, (c) 0.12, and (d) 0.25 samples. The inset shows the corresponding enlarged version near the susceptibility peak.

volume fraction of the slowly fluctuating clusters with increase in temperature could be the possible origin for the observed reverse trend in T_P shift. Similar behavior has been observed for the itinerant ferromagnet $SrRuO_3$ and antiferromagnetic $NaNiO_2$ [25,26].

Interestingly, the T_P values observed in $(LSMO)_{1-x}(BTO)_x$ solid solutions are relatively at high temperatures (>240 K for all the compounds except for $x = 0.25$) in comparison to the B-site-doped $La_{1-x}Sr_xMnO_3$ systems [15,16], where the reentrant SG state is reported with T_P below 150 K. The canonical SG behavior can be explained by three basic models, the Vogel-Fulcher (VF), Néel-Arrhenius (NA), and slow dynamics models. The -dependence of the T_P with this reverse trend cannot be fitted to the VF, NA, and slow dynamics models and thus excludes the canonical SG behavior in our system.

However, when the interparticle magnetic dipole interaction (in a super-spin-glass) among the concentrated nanoparticles is significant, magnetic properties similar to SG behavior are observed [27,28]. The interparticle dipolar interaction is well explained by the Dormann-Bessais-Fiorani (DBF) model [27] and the modified relaxation time given by this model is expressed as $\tau = \tau_0 \exp[\frac{E_a + E_{int}}{k_B T_P}]$ where E_a is the anisotropy energy, k_B is the Boltzmann constant, E_{int} is the interaction energy, and τ_0 is the microscopic spin-flip time. As per the DBF model, the response time should increase with decreasing temperature. However, the experimental data plotted in Fig. 7 show the opposite trend, i.e., decrease of response time with decrease of temperature and thus exclude the DBF model for the observed behavior. Additionally, the average particle sizes of all the samples are in the range of 35 to 45 nm which in turn decrease the anisotropy energy due to the multidomain formation [14]. This excludes the "superspin" concept as it is applicable to single-domain magnetic particles (average particle diameter ~10 nm) [20]. Alternatively, we expect that the breaking of long-range symmetry could be one possible reason for the SG state in our systems.

D. Memory effect

To get further insight into the SG state, we have carried out time-dependent memory experiments [29–32]. This is done by performing the ac susceptibility measurements in two ways, first in the halting mode (χ'_{mem}) and second in the reference mode (χ'_{ref}). In halting mode, the sample is zero-field cooled from 300 K to the lowest temperature with an intermediate halt (t_{halt}) at the halting temperature (T_{halt}) for a period of time t and the (χ'_{mem}) is recorded during the heating cycle at a rate of 2 K/min under a probing ac field of $H_{ac} = 170$ mOe and frequency $f = 420$ Hz. In the reference mode, the experiment is performed using the same protocol but without any halting

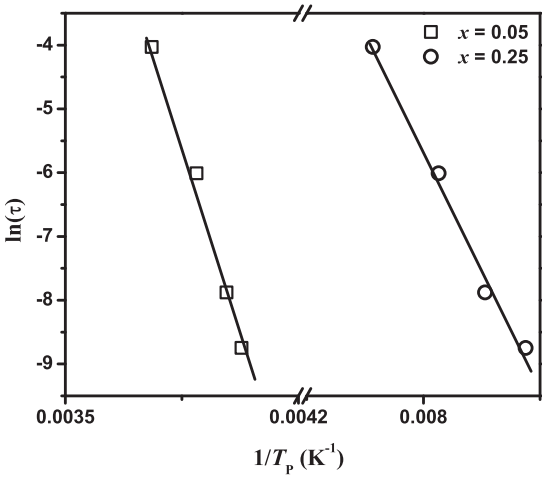

FIG. 7. Response time as a function of $1/T_P$ for $x = 0.05$ and 0.25 samples (the solid lines are drawn as guides to the eye).

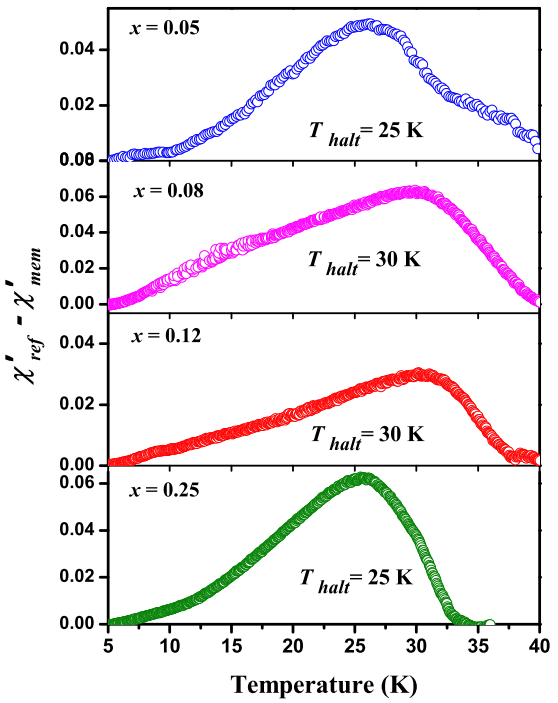

FIG. 8. The $\Delta\chi\prime[=(\chi'_{\rm ref}-\chi'_{\rm mem})]$ versus temperature graph for $x = 0.05, 0.08, 0.12$ and 0.25 samples.

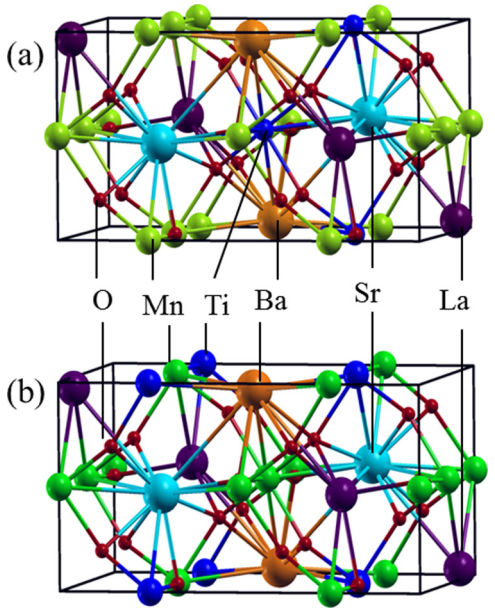

FIG. 9. Supercell structure of LSMO-BTO composition expanded along [100] direction. (a) Ba follows Ti and therefore BTO remains as a single perovskite unit. (b) Ba and Ti ions are separated.

$t_{\rm halt}$, and the $(\chi'_{\rm ref})$ is measured during the heating cycle using the same measuring parameters as for $\chi\prime_{\rm mem}$. Here, the $\chi'_{\rm mem}(T)$ and $\chi'_{\rm ref}(T)$ are recorded with $T_{\rm halt}$ at 25 K for $x = 0.05$, 0.25, and at 30 K for $x = 0.08$, 0.12 samples by keeping the $t_{\rm halt} = 12$ h for all samples. Generally, aging and memory effects are time-dependent phenomena common in disordered glassy systems. The system never achieves the equilibrium state within the experimental time scale. To ascertain the memory effect, the difference in susceptibility $\Delta\chi\prime = (\chi'_{\rm ref} - \chi'_{\rm mem})$ is plotted as a function of T and shown in Figs. 8(a) to 8(d) for the $x = 0.05, 0.08, 0.12$, and 0.25 samples. The observed maximum in $\Delta\chi\prime$ at $T_{\rm halt}$ confirms the memory effect in the samples, which in turn is attributed to the SG state of the systems. The depth of the memory can be quantified by the factor $\Delta T/T_{\rm P}$, where ΔT is the full width at half maximum of the $\Delta\chi'$ versus T curve and $T_{\rm P}$ is the glass transition temperature (the high-frequency maximum in the χ' versus T curve) [19,33,34]. The ΔT obtained from the $\Delta\chi'$ versus T curve and the percentage $(\Delta T/T_{\rm P})$ measured in relative units for the $x = 0.05, 0.08, 0.12$, and 0.25 samples are given in Table I. Although the percentage $\Delta T/T_{\rm P}$ value is low compare to those in ferrofluids [34], alloys [35], and granular films [36], it attains significance compared to similar such systems [25] where the detailed memory effect is not clearly established.

TABLE I. The peak temperature $T_{\rm P}$, full widths at half maximum ΔT, and percentage $(\Delta T/T_{\rm P})$ are listed for various compositions x.

x	$T_{\rm P}$ (K)	ΔT	$\Delta T/T_{\rm P}(\%)$
0.05	251	15.6	6.4
0.08	266	11.3	4.5
0.12	241	9.3	3.9
0.25	119	7.8	6.9

IV. GROUND STATE MAGNETIC STRUCTURE FROM DENSITY-FUNCTIONAL CALCULATIONS

A. Computational details

Density-functional calculations are performed on the $(LSMO)_{0.75}(BTO)_{0.25}$ sample, which has the maximum composition among the solid solutions in the present investigation, as it shows unambiguous SG behavior. Two sets of supercells were constructed with the first one constituted of 40 atoms and the second one constituted of 80 atoms to carry out the DFT calculations for different purposes such as determining the electronic properties, magnetic configurations, and Ti segregation. The supercells are constructed by repeating the experimental *Pbnm* structure of LSMO (20-atom unit cell) along either of the translation vectors twice or four times as can be seen from Figs. 9 and 13, respectively. For the 40- (80-) atom supercell, two (four) of the La/Sr ions are replaced by Ba ions and two (four) of the Mn ions are replaced by Ti ions to realize 25 % BTO concentration. Even though the experimental LSMO sample has 30 % Sr concentration, here we have considered 25 % Sr concentration for supercell convenience. Based on the magnetic phase diagram of LSMO [37], the 25 % concentration also favors strong ferromagnetic ordering and therefore the results discussed in this section can be used to support the experimental studies of the previous section.

A full-potential linearized augmented plane wave method with the local orbital (LO) as additional basis (LAPW+LO) is employed to solve the Kohn-Sham equation self-consistently

using the WIEN2K package [38]. Exchange correlation is approximated through the generalized gradient approximation (GGA) [39] and the strong-correlation effect in this oxide system is taken into account through the effective Hubbard $U(U_{\text{eff}} = U - J \sim 3$ eV) [40]. The Brillouin zone integration is carried out using the tetrahedron method though a $4 \times 6 \times 8$ k mesh to achieve self-consistency with the desired accuracy for the 40-atom ($2 \times 1 \times 1$) supercell. For any other supercell an appropriate k mesh is constructed. The LAPW basis functions include $2s$ and $2p$ orbitals for O; $5s$ and $6s$ orbitals, respectively, for Sr and Ba; $6s$ and $5d$ orbitals for La; and $3d$ and $4s$ orbitals for the transition metal elements. The $R_{\text{mt}}K_{\text{max}}$ is taken as 7 to decide the momentum cutoff which resulted in 4491 basis functions and 95 893 plane waves at each k point.

B. Electronic structure of $La_{0.75}Sr_{0.25}MnO_3$

In this section we discuss the DFT-obtained electronic structure of LSMO, although it is already established in the literature [41,21], for completeness as well as to bring perspective to the electronic structure of $(LSMO)_{1-x}(BTO)_x$ solid solutions which is the focus of this paper. The spin-resolved total and orbital-projected Mn-d densities of states (DOSs) and the band structure in the vicinity of the Fermi level (E_F) are shown in Fig. 10. The most important aspect of the electronic structure of LSMO that we infer from this figure is the splitting of Mn-d states to triply degenerate t_{2g} and doubly degenerate e_g states due to the octahedral crystal field of the MnO_6 complex. While t_{2g} states are localized and completely occupied in one spin channel to behave like classical spins, the e_g states are dispersive and partially occupied. From our calculation we estimate the e_g occupancy to be around 0.38 per Mn atom. Mean-field Hartree-Fock calculations suggest that an occupancy of 0.2 is sufficient to stabilize the ferromagnetic ground state via the double-exchange mechanism [42]. Also our DFT results, in agreement with the earlier studies [41,21], predict LSMO to be a half-metallic ferromagnet.

C. Electronic structure of $(LSMO)_{0.75}(BTO)_{0.25}$

For computational purposes, we considered a supercell consisting of eight primitive unit cells**,** where four $LaMnO_3$ formula units (f.u.), two $SrMnO_3$ f.u., and two $BaTiO_3$ f.u. are accommodated. Even though we have a supercell structure, the best possible uniform distribution of La and Sr ions is made to bring it close to the experimental LSMO configuration.

To gain insight into the magnetic stability of $(LSMO)_{0.75}(BTO)_{0.25}$ we have considered three magnetic orderings: (I) ferromagnetism (FM), where the spins of transition metal ions are aligned along the same direction, (II) G-type antiferromagnetism (G-AFM), where neighboring spins are antiparallel, and (III) A-type antiferromagnetism (A-AFM) where spins are parallel in the xy plane and antiparallel along the z axis. The local magnetic moments at the transition metal sites and the total energy for each of the configurations, both for LSMO and $(LSMO)_{0.75}(BTO)_{0.25}$, are mentioned in Table II. Two important observations are made from the Table II. (A) FM ordering is the most stable structure for both LSMO and $(LSMO)_{0.75}(BTO)_{0.25}$ and both of them are half metallic.

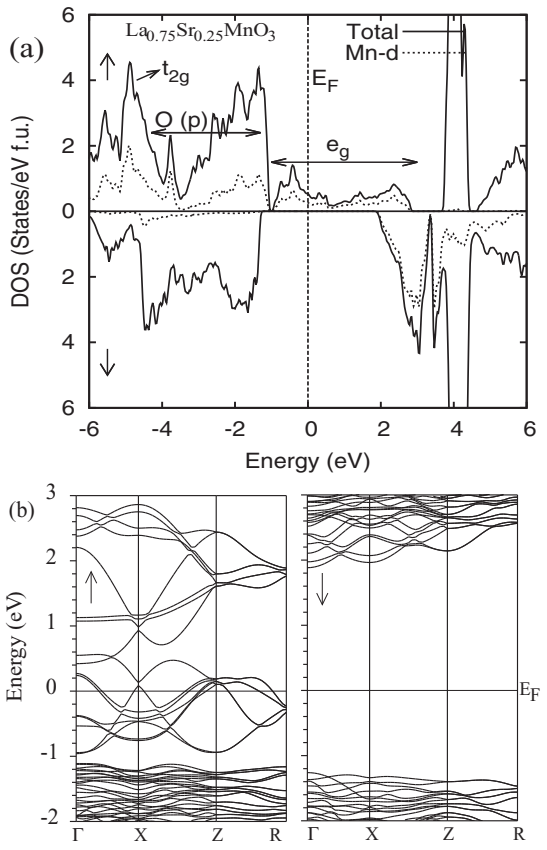

FIG. 10. (a) Total and Mn-d DOSs for $La_{0.75}Sr_{0.25}MnO_3$ (LSMO). Arrows indicate the respective spin channel. (b) Spin-up and spin-down band structures near E_F. Both DOS and band structure demonstrate the partial occupancy of delocalized e_g states as well as half metallicity.

However, in contrast to LSMO, in $(LSMO)_{0.75}(BTO)_{0.25}$ the G-AFM structure is more stable than the A-AFM structure. This is due to the fact that the A-AFM structure becomes more favorable with increase in La concentration. In fact the ground state of $LaMnO_3$ has A-AFM ordering [4]. With decreasing La concentration, the Mn charge state moves from 3+ to 4+, which favors the G-AFM structure [43]. (B) There is a very small magnetic moment (of the order $0.02\,\mu_B$) at the Ti site indicating that Ti still remains nonmagnetic and in the 4+ charge (d^0) state which is also reflected in the Ti-d DOS plot shown in Fig. 11. As a result, the magnetic exchange interactions among the Mn spins are broken whenever there is a Ti ion at the intermediate position. The average spin exchange J is estimated by calculating the difference between the FM and AFM ordering of the core-spins' ground state energies (per formula unit):

$$J = E_{\uparrow\uparrow} - E_{\uparrow\downarrow} \ldots,. \quad (1)$$

Since the DFT calculations are carried out for an ordered structure, instead of a random structure, due to the supercell geometry there will be a variation of exchange interactions across the sites. Therefore, average values are estimated and shown in Fig. 12. The results are comparable to the earlier reported results on LSMO [21]. The figure shows that while the strength of the ferromagnetic ordering is not affected by

TABLE II. Stability of FM, A-AFM, and G-AFM configurations in LSMO and $(LSMO)_{0.75}(BTO)_{0.25}$. From total energies (per 20 atom formula unit), written in the second and fourth columns, the FM configuration is found to be the ground state for both the systems. The average values of the local magnetic moments at Mn and Ti sites corresponding to different configurations are also listed.

	LSMO		$(LSMO)_{0.75}(BTO)_{0.25}$		
Magnetic structure	Energy (meV)	Mn moment (μ_B)	Energy (meV)	Mn moment (μ_B)	Ti moment (μ_B)
FM	0	3.45	0	3.40	0.02
A-AFM	111	3.31	127	3.30	0
G-AFM	139	3.33	87	3.27	0.03

the doping of BTO, the Mn and Ti do not have any magnetic interactions due to lack of spin moment formation at the latter site. During the synthesis process it may happen that BTO does not remain as a single perovskite unit in the LSMO matrix. Therefore, we have considered a distribution where Ba does not follow Ti as shown in Fig. 9(b). The partial density of states for this distribution are shown in Fig. 11(b). While there is a small modification in the Mn-*d* DOS near E_F compared to the previous distribution, there is no change in the Ti-*d* DOS.

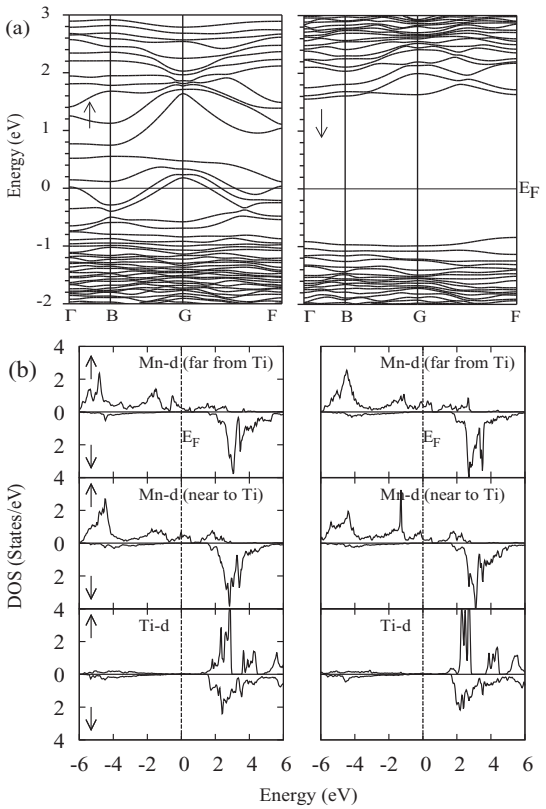

FIG. 11. (a) Spin-polarized band structure of $(LSMO)_{0.75}(BTO)_{0.25}$ retaining the half-metallic feature of the undoped LSMO. (b) Mn and Ti-*d* DOSs for the $(LSMO)_{0.75}(BTO)_{0.25}$ compound in its ground state. The left and right panels of (b) correspond to the supercells shown in Figs. 9(a) and 9(b), respectively. In both the cases, Ti-*d* states are almost unoccupied to stabilize in a d^0 configuration. Although Mn-*d* valence densities of states close to the Fermi level are slightly depleted, the overall feature remains the same as in the case of LSMO.

The half-metallic behavior is also not affected by this new distribution.

D. Short-range magnetic domains and Ti ion segregation; SG behavior

The DFT results presented so far reveal that nonmagnetic Ti acts as a barrier against interaction between the Mn spins. However, the Mn spins in their close proximity remain parallel (see Fig. 12) as in the case of LSMO. This implies that if short-range Mn domains can be created through Ti segregation, each domain will have FM ordering, but the spin orientation might differ in each domain. To see the possibilities of Ti segregation, we designed several supercells by repeating the orthorhombic unit cell along [100], [010], and [001] and in each supercell we changed the distribution of Ba and Ti ions in the LSMO matrix as shown in Fig. 13. The ground state distribution for each supercell is obtained through total-energy calculations.

Figure 13 shows that for each of the supercells the ground state distribution is the one where the Ti ions are close to each other, which suggests Ti segregation in LSMO-BTO. The segregation energy E(Ti near)$-E$(Ti far) is found to be more negative (~ -1.7 eV) for the $(1 \times 1 \times 4)$ supercell with $AO-BO_2$ layered geometry. However, the segregation energy is also significantly negative (~ -0.43 eV) for the other nonlayered supercells $(4 \times 1 \times 1)$ and $(1 \times 4 \times 1)$. Therefore, our calculations primarily emphasize that, based on the growth conditions and synthesis procedures, there will be many local minima favoring Ti segregation in directions other than [001]. Furthermore, to see whether the Ba ion necessarily follows the Ti ion to stay as a single BTO unit in the LSMO matrix, we

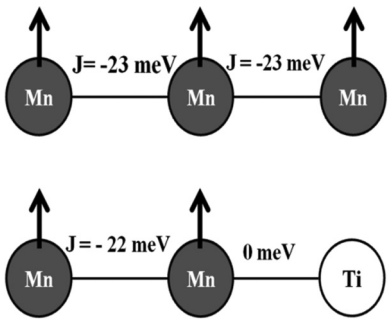

FIG. 12. Exchange interactions among the Mn spins with and without the presence of Ti ion. The results are obtained using Eq. (1) and Table I.

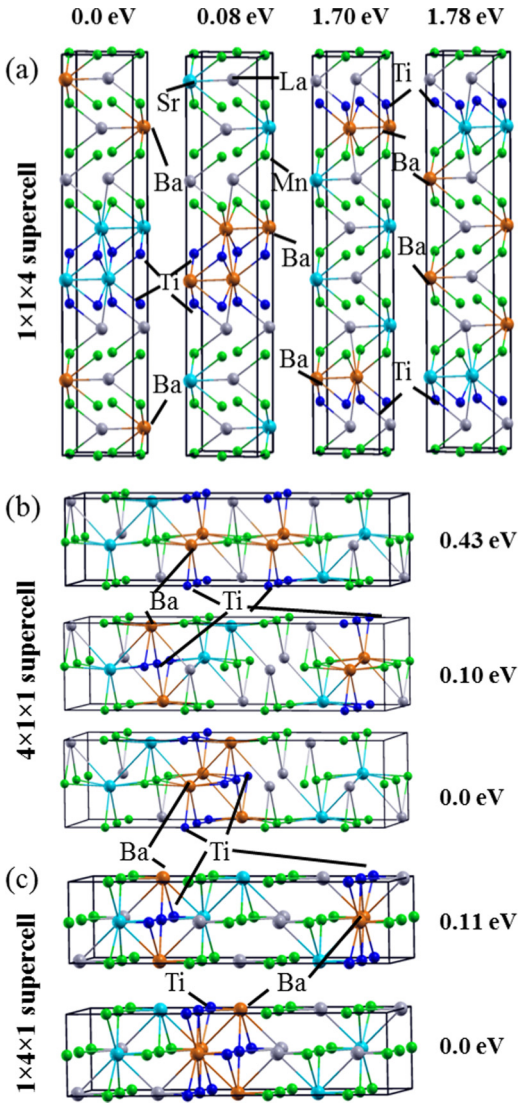

FIG. 13. Supercells representing $(LSMO)_{0.75}(BTO)_{0.25}$ with different Ba and Ti (spatial) distributions. Oxygen atoms are removed from the structure to improve the clarity. (a) $1 \times 1 \times 4$ supercell with four different distributions, (b) $4 \times 1 \times 1$ supercell with three different distributions, and (c) $1 \times 4 \times 1$ supercell with two different distributions. Relative energy of each distribution with respect to the minimum one in a given supercell is also mentioned.

calculated the total energy by keeping the Ba and Ti ions away from each other and together in the $(1 \times 1 \times 4)$ supercell as shown in Fig. 13. Staying as a BTO unit is found to be less stable by a small amount of energy of 0.08 eV. The situation might change with change in the supercell orientation.

Figures 12 and 13 collectively imply the formation of short-range Mn domains separated by Ti barriers as schematically illustrated in Fig. 1. Each domain will have FM ordering. However, as one domain is not affected by the other due to the broken exchange interaction the spin orientation of each domain can vary. This leads to the SG behavior in LSMO-BTO as demonstrated by the experimental studies.

V. CONCLUSIONS

The nanoparticulate single phase $(LSMO)_{1-x}(BTO)_x$ ($x = 0.0, 0.05, 0.08, 0.12,$ and 0.25) solid solutions are synthesized by the usual sol-gel route. The obtained nanopowders are characterized for their magnetic properties. The large deviation in magnetization data between the FC and ZFC temperature-dependent magnetization measurements, unsaturated spontaneous magnetization even at high external magnetic field, and the temperature-dependent ac susceptibility data at different frequencies strongly indicate SG states in the $(La_{0.7}Sr_{0.3}MnO_3)_{1-x}(BaTiO_3)_x$ system. However, the inverse frequency dependence of the susceptibility peak temperature may originate from the complex temperature-dependent freezing of the magnetic domains within the nanoparticles. The memory effect measurements further ascertain the SG state in the system. Ironically the observed spin-glass states are not behaving like the normal canonical SG state and do not fit well with the existing known models. The glassy behavior in this system could be due to the SG state that arises due to the temperature-dependent interacting domains within the nanoparticles. The DFT calculations carried out on these systems reveal that the parent LSMO and the $(LSMO)_{1-x}(BTO)_x$ solid solutions are half metallic in nature with a ferromagnetic stable ground state. The calculations lead to the conclusion that the Ti^{4+} ions indeed break the long-range ferromagnetic ordering of Mn spins and thereby induce the SG state in the system by forming short-range ferromagnetic domains.

[1] Y. Tokura and Y. Tomioka, J. Magn. Magn. Mater. **200**, 1 (1999).
[2] M. Bowen, M. Bibes, A. Barthélémy, J.-P. Contour, A. Anane, Y. Lemaître, and A. Fert, Appl. Phys. Lett. **82**, 233 (2003).
[3] P. Raychaudhuri, K. Sheshadri, P. Taneja, S. Bandyopadhyay, P. Ayyub, A. K. Nigam, R. Pinto, S. Chaudhary, and S. B. Roy, Phys. Rev. B **59**, 13919 (1999).
[4] M. Imada, A. Fujimori, and Y. Tokura, Rev. Mod. Phys. **70**, 1039 (1998).
[5] C. A. F. Vaz, J. Hoffman, Y. Segal, J. W. Reiner, R. D. Grober, Z. Zhang, C. H. Ahn, and F. J. Walker, Phys. Rev. Lett. **104**, 127202 (2010).
[6] A. G. Lehmann, C. Sanna, F. Congiu, G. Concas, and L. Maritato, Phys. Status Solidi B **246**, 1948 (2009).
[7] G. Srinivasan, Annu. Rev. Mater. Res. **40**, 153 (2010).
[8] H. Lu, T. A. George, Y. Wang, I. Ketsman, J. D. Burton, C. -W. Bark, S. Ryu, D. J. Kim, J. Wang, C. Binek, P. A. Dowben, A. Sokolov, C.-B. Eom, E. Y. Tsymbal, and A. Gruverman, Appl. Phys. Lett. **100**, 232904 (2012).
[9] C. A. F. Vaz, Y. Segal, J. Hoffman, R. D. Grober, F. J. Walker, and C. H. Ahn, Appl. Phys. Lett. **97**, 042506 (2010).
[10] X. K. Ning, Z. J. Wang, and Z. D. Zhang, Adv. Funct. Mater. **24**, 5393 (2014).
[11] J. F. Ding, O. I. Lebedev, S. Turner, Y. F. Tian, W. J. Hu, J. W. Seo, C. Panagopoulos, W. Prellier, G. Van Tendeloo, and T. Wu, Phys. Rev. B **87**, 054428 (2013).

[12] V. Markovich, I. Fita, A. Wisniewski, G. Jung, D. Mogilyansky, R. Puzniak, L. Titelman, and G. Gorodetsky, Phys. Rev. B **81**, 134440 (2010).
[13] T. Zhu, B. G. Shen, J. R. Sun, H. W. Zhao, and W. S. Zhan, Appl. Phys. Lett. **78**, 3863 (2001).
[14] S. Roy, I. Dubenko, D. D. Edorh, and N. Ali, J. Appl. Phys. **96**, 1202 (2004).
[15] B. Aslibeiki, P. Kameli, and H. Salamati, Solid State Commun. **149**, 1274 (2009).
[16] P. T. Phong, D. H. Manh, N. X. Phuc, and I.-J. Lee, Physica B **408**, 22 (2013).
[17] K. Manna, D. Samal, S. Elizabeth, H. L. Bhat, and P. S. Anil Kumar, J. Supercond. Nov. Magn. **24**, 833 (2011).
[18] Y.-K. Tang, Y. Sun, and Z. -H. Cheng, Phys. Rev. B **73**, 012409 (2006).
[19] J. A. De Toro, S. S. Lee, D. Salazar, J. L. Cheong, P. S. Normile, P. Muniz, J. M. Riveiro, M. Hillenkamp, F. Tournus, A. Tamion, and P. Nordblad, Appl. Phys. Lett. **102**, 183104 (2013).
[20] J. A. D. Toro, P. S. Normile, S. S. Lee, D. Salazar, J. L. Cheong, P. Muñiz, J. M. Riveiro, M. Hillenkamp, F. Tournus, A. Tamion, and P. Nordblad, J. Phys. Chem. C **117**, 10213 (2013).
[21] B. R. K. Nanda and S. Satpathy, Phys. Rev. B **79**, 054428 (2009).
[22] C. Zener, Phys. Rev. **82**, 403 (1951).
[23] E. Wimmer, H. Krakauer, M. Weinert, and A. J. Freeman, Phys. Rev. B **24**, 864 (1981).
[24] P. A. Yadav, A. V. Deshmukh, K. P. Adhi, B. B. Kale, N. Basavaih, and S. I. Patil, J. Magn. Magn. Mater. **328**, 86 (2013).
[25] C. Sow, D. Samal, P. S. Anil Kumar, A. K. Bera, and S. M. Yusuf, Phys. Rev. B **85**, 224426 (2012).
[26] P. J. Baker, T. Lancaster, S. J. Blundell, M. L. Brooks, W. Hayes, D. Prabhakaran, and F. L. Pratt, Phys. Rev. B **72**, 104414 (2005).
[27] S. Nakamae, C. Crauste-Thibierge, D. L'Hôte, E. Vincent, E. Dubois, V. Dupuis, and R. Perzynski, Appl. Phys. Lett. **101**, 242409 (2012).
[28] K. Hiroi, K. Komatsu, and T. Sato, Phys. Rev. B **83**, 224423 (2011).
[29] M. H. Ehsani, P. Kameli, M. E. Ghazi, and F. S. Razavi, Adv. Mater. Res. **829**, 712 (2014).
[30] D. Samal and P. S. Anil Kumar, J. Phys.: Condens. Matter. **23**, 016001 (2011).
[31] K. Manna, D. Samal, S. Elizabeth, H. L. Bhat, and P. S. Anil Kumar, J. Phys. Chem. C **115**, 13985 (2011).
[32] A. K. Kundu, P. Nordblad, and C. N. R. Rao, Phys. Rev. B **72**, 144423 (2005).
[33] S. Sahoo, O. Petracic, W. Kleemann, P. Nordblad, S. Cardoso and P. P. Freitas, Phys. Rev. B **67**, 214422 (2003).
[34] P. E. Jönsson, H. Yoshino, H. Mamiya, and H. Takayama, Phys. Rev. B **71**, 104404 (2005).
[35] M. Osth, D. Herisson, P. Nordblad, J. A. De Toro, and J. M. Riveiro, J. Magn. Magn. Mater. **313**, 373 (2007).
[36] J. Du, B. Zhang, R. K. Zheng, and X. X. Zhang, Phys. Rev. B **75**, 014415 (2007).
[37] Yufeng Tian, Siadur Rahman, and Tom Wu, Nanoscale **4**, 1529 (2012).
[38] P. Blaha, K. Schwarz, G. K. H. Madsen, D. Kvasnicka, and J. Luitz, *Computer Code* WIEN2K, *an Augmented Plane Wave Plus Local Orbitals Program for Calculating Crystal Properties* (Vienna University of Technology, Austria, 2001).
[39] J. P. Perdew, K. Burke, and M. Ernzerhof, Phys. Rev. Lett. **77**, 3865 (1996).
[40] V. I. Anisimov, J. Zaanen, and O. K. Andersen, Phys. Rev. B **44**, 943 (1991).
[41] C. Ma, Z. Yang, and S. Picozzi, J. Phys.: Condens. Matter **18**, 7717 (2006).
[42] B. R. K Nanda, S. Satpathy, and M. S. Springborg, Phys. Rev. Lett. **98**, 216804 (2007).
[43] J. Hemberger, A. Krimmel, T. Kurz, H.-A. Krug von Nidda, V. Yu. Ivanov, A. A. Mukhin, A. M. Balbashov, and A. Loidl, Phys. Rev. B **66**, 094410 (2002).